Frequency and Polarization Agile RFID Patch Antenna with Reduced Dimensions

Original
Frequency and Polarization Agile RFID Patch Antenna with Reduced Dimensions / Tolin, Enrico; Vipiana, Francesca; Bahr, Achim; Bruni, Simona; Simon, Winfried. - ELETTRONICO. - (2019). (2019 IEEE International Symposium on Antennas and Propagation and USNC-URSI Radio Science Meeting Atlanta, Georgia, USA 7-12 July 2019) [10.1109/APUSNCURSINRSM.2019.8888687].

Availability:
This version is available at: 11583/2760742 since: 2020-07-03T13:25:35Z

Publisher:
Institute of Electrical and Electronics Engineers Inc.

Published
DOI:10.1109/APUSNCURSINRSM.2019.8888687

Improved Outdoor Target Tracking via EKF-based GNSS/UWB Tight Integration with Online Time Synchronisation

Yihan Guo, Oliviero Vouch, Simone Zocca, Alex Minetto, Fabio Dovis
Department of Electronics and Telecommunications (DET), Politecnico di Torino (Turin, Italy)

BIOGRAPHY

Yihan Guo was born in Xianyang, China, in 1994. He received the B.Sc. degree from Northwestern Polytechnical University, China, in 2016, and the M.Sc. degree from Shanghai Jiaotong University, China, in 2019. He is a Ph.D. student in Politecnico di Torino, Italy, and also a member of the Navigation Signal Analysis and Simulation (NavSAS) research group. His current research interests include integrated navigation systems based on Global Navigation Satellite System (GNSS) and Ultra-Wideband (UWB).

Oliviero Vouch was born in Casale Monferrato, Italy, in 1996. He received the B.Sc. degree in Electronics and Communications Engineering (ECE) in 2018 and the M.Sc. degree in Communications and Computer Networks Engineering (CCNE) in 2020, both from Politecnico di Torino, Turin, Italy. He joined the Department of Electronics and Telecommunications (DET) of Politecnico di Torino as a PhD student in 2021 and he is member of the Navigation Signal Analysis and Simulation (NavSAS) research group. His academic background includes advanced signal processing and his current research interests cover advanced Bayesian estimation applied to navigation sensors integration.

Simone Zocca was born in Torino, Italy, in 1995. He received a B.Sc. in Telecommunication Engineering in 2018 and a M.Sc. in Communication and Computer Networks Engineering in 2020, both from Politecnico di Torino. He is currently a Ph.D. student within the NavSAS research group (Navigation Signal Analysis and Simulation) at the Department of Electronics and Telecommunications in Politecnico di Torino. His research is focused on innovative solutions for signal processing techniques and Bayesian estimation applied to global navigation satellite system (GNSS).

Alex Minetto was born in Pinerolo, Italy, in 1990. He received the B.Sc. and M.sc. degrees in Telecommunications Engineering from Politecnico di Torino, Turin, Italy and his Ph.D. degree in Electrical, Electronics and Communications Engineering, in 2020. He joined the Department of Electronics and Telecommunications of Politecnico di Torino in 2019 as research and teaching assistant. In 2015 he spent a six-month internship at European Organisation for the Exploitation of Metereological Satellites (EUMETSAT), Darmstadt, Germany. His current research interests cover signal processing and advanced Bayesian estimation applied to Global Navigation Satellite System (GNSS) cooperative receivers.

Fabio Dovis was born in Bruino, Italy, in 1970. He received the M.Sc. degree in electronics engineering and Ph.D. degree in electronics and communications engineering from Politecnico di Torino, Turin, Italy, in 1996 and 2000, respectively. He was with the Department of Electronics and Telecommunications, Politecnico di Torino, as an Assistant Professor in 2004 and since 2014, he has been Associate Professor with the Department of Electronics and Telecommunications, Politecnico di Torino, where he coordinates the Navigation Signal Analysis and Simulation research group. He has a relevant experience in European projects in satellite navigation as well as cooperation with industries and research institutions. His research interests include the design of GPS and Galileo receivers and advanced signal processing for interference and multipath detection and mitigation, as well as ionospheric monitoring. Mr. Dovis is a member of the IEEE AEROSPACE AND ELECTRONICS SYSTEMS SOCIETY NAVIGATION SYSTEMS PANEL.

ABSTRACT

Accurate and robust positioning technology in the mass-market segment is pivotal to support a number of critical Positioning, Navigation and Timing (PNT) applications. State-of-the-art Global Navigation Satellite System (GNSS) receivers design has been increasingly targeting flexible, embedded architectures integrating low-cost sensors to overcome GNSS limitations. The widespread proliferation of Ultra-Wide Band (UWB) technology, which enables centimeter-level accurate ranging in cluttered environments, is an appealing candidate for tight hybridisation with GNSS. When dealing with data streams from different Commercial-Off-The-Shelf (COTS) sensors, it is known that temporal misalignment is of concern, and accurate state-estimation via centralised, recursive filtering architectures can be undermined. As a first contribution, this work theoretically analyses the accuracy impact of asynchronous data association in the framework of a tightly integrated GNSS/UWB system leveraging plain Extended Kalman Filter (EKF) integration. Then, it puts forward a novel EKF-based model implementing online time offset estimation and compensation (i.e., time calibration) for GNSS/UWB tight integration. Results obtained in a multi-agent, cooperative scenario demonstrate that the proposed hybridisation methodology can achieve horizontal and vertical positioning accuracy gains of $33.95\,\%$ and $59.33\,\%$, respectively, in Root-Mean-Square Error (RMSE) terms.

I. INTRODUCTION

The growing number of mass-market applications requiring geo-positioning capabilities have stimulated an ever-increasing rollout of Positioning, Navigation and Timing (PNT) services based on Global Navigation Satellite Systems (GNSSs), and technology trends at a global scale are steadily pushing the boundaries of the perfromance constraints posed on GNSS-based navigation units (European GNSS Agency - GSA, 2020). In the sphere of high-volume devices, multi-frequency, multi-constellation signal processing, combined with the increased use of correction services, has now become state-of-the-art, but smarter design solutions are required for consumer GNSS chipsets to contribute to the assured and reliable positioning and guidance of agents (Morton et al., 2020). In fact, in challenging navigation environments (e.g., deep urban contexts or wooded areas), GNSS signal availability is often compromised and dominant error sources such as multipath and shadowing effects hinder accurate GNSS-only Position, Velocity, Timing (PVT) solutions (Kaplan and Hegarty, 2017; McGraw et al., 2021; Zhu et al., 2018). Among the options, modern PNT units are increasingly targeting flexible, integrated architectures fusing complementary navigation sensors to low-cost GNSS (Cristodaro, 2019; Vouch et al., 2021; Maaref and Kassas, 2020).

Ultra-Wide Band (UWB) technology is of growing interest for hybridisation with GNSS signals. Over short distances, UWB has great potential in terms of multipath resilience and suppression of reflected signals; the Radio Frequency (RF) transmission of non-sinusoidal pulses with nanosecond lifetime and spread-spectrum features ensures good obstacle penetration capabilities and high time resolution (Zekavat and Buehrer, 2019; Dardari et al., 2009; Win and Scholtz, 1998). Hence, Two-Way Time-Of-Flight (TWTOF) communication between UWB transceivers can achieve sub-centimetre accurate ranging in dense, cluttered environments. For outdoor applications, GNSS/UWB fusion can be leveraged to deliver enhanced PNT capabilities in terms of accuracy and continuity of operations criteria. On-site deployment of geo-referenced UWB modules, acting as opportunistic environment landmarks, can offer a local infrastructure of ranging augmentation to improve absolute and relative localisation in areas with limited GNSS availability (Gross et al., 2015). Although examples of loose coupling between GNSS and UWB exist (Cebrian et al., 2019), GNSS/UWB tight integration would be preferable for manifold reasons (Falco et al., 2017). (Johnson and Dewberry, 2011) was a pioneering research proposing a UWB-based ranging augmentation, under accurate landmarks registration, for a GNSS/UWB system exploiting distributed Extended Kalman Filter (EKF)-based tight integration. Other more recent contributions dealing with Vehicle-to-everything (V2X) applications, then, presented hybrid strategies combining the benefits of Cooperative Positioning (CP), Carrier-phase-based Real-Time Kinematic (RTK) and UWB ranging to accomplish decimeter-level accurate urban navigation (Gao et al., 2014; Zhuang et al., 2021). As a pilot study, this work addresses GNSS/UWB tight integration in the framework of a multi-agent, cooperative scenario where the absolute positioning of an Unmanned Ground Vehicle (UGV) is assisted by an Unmanned Aerial Vehicle (UAV) enabling UWB-based relative ranging as a local pseudolite.

Recursive Bayesian filters for centralised GNSS/UWB data fusion assume accurately timestamped and synchronised measurements from different sensors to deliver accurate and trustworthy estimation of the state of a tracked dynamic system (Caceres Duran et al., 2012; Veth, 2021). However, when tightly integrating low-cost UWB sensors to a GNSS receiver, Commercial-Off-The-Shelf (COTS) chipsets have independent, asynchronous clocks. Therefore, GNSS and UWB measurements are tagged to time-scales that are misaligned to each other. Moreover, a lag exists between the measurements' timestamp and each time instant when the integration filter (also known as hybridisation, or navigation filter) processes the available GNSS and UWB measurements. In particular, this lag is different for GNSS and UWB because sampling rates are different and clocks are independent. On top of that, unmodelled timing disturbances such as spurious clock drifts can even impact the timestamping precision with respect to the true instant measurements are dumped. In light of the foregoing, an unknown time-offset factor exists between the GNSS timestamps and the UWB timestamps which models both the relative shift between the GNSS and the UWB time-scales and the offset of these scales with respect to the hybridisation filter time-scale (Julier and Uhlmann, 2005). This time-offset can inject an inconsistency bias inside the integration filter model which curbs accurate state-estimation (Skog and Handel, 2011; Qin and Shen, 2018).

The problem of time-synchronisation can be handled from different perspectives. Hardware synchronisation typically exploits the GNSS Pulse-Per-Second (PPS) timing signal as a triggering source, and cross-referencing of the timing signals from the fused sensors is achieved to establish a shared event base in the integration engine (Ding et al., 2008). However, direct synchronisation is often unfeasible with COTS components because the access to the hardware is limited. For centralised measurement fusion architectures, synchronisation is often addressed as a time calibration task (Kelly and Sukhatme, 2014). (Rehder et al., 2016) have studied the estimation of temporal offsets among self-contained sensor units as a maximum likelihood optimisation problem. Other optimisation-based strategies for multisensor calibration have been investigated in (Huang et al., 2021; Peršić et al., 2021). In this work, inspired by contributions outside GNSS literature (Kelly et al., 2021; Li and Mourikis, 2013), filtering-based time calibration is considered for the tight integration problem under study, which requires the modelling of the unknown GNSS/UWB time-offset as part of the hybridisation filter model; this way, a new measurement function is achieved and the actual temporal misalignment between sensors can be estimated jointly with the other states given a convenient state-space formulation (Nilsson et al., 2010).

As a matter of fact, for navigation applications involving low kinematics agents, few tens of milliseconds of temporal misalignment produce a negligible impact on the accuracy of the integrated solution. By contrast, under higher kinematics, uncompensated time-offsets can translate into meters of positioning error. Among the contributions of this paper, positioning accuracy degradation caused by uncalibrated GNSS/UWB time-offset is explored for a tight integration leveraging plain EKF (Julier and Uhlmann, 1997). Then, a GNSS/UWB tight integration model embedding time-offset calibration via EKF filtering is formulated. The proposed methodology is assessed via simulation-based analysis in order to both demonstrate the improved positioning accuracy against plain EKF integration and to validate its applicability in the context of the aforementioned UGV-UAV multi-agent, cooperative scenario.

The remainder of this paper is organized as follows: Section II not only illustrates a convenient time-offset modelling for GNSS/UWB hybridisation, but also provides the measurement models of GNSS and UWB. Then, Section III presents a GNSS/UWB tight integration model with time-offset calibration and analyses the time-offset's impact on positioning results. Simulation-based experimental results are presented and discussed in Section IV. Eventually, Section V provides relevant conclusions about this pilot research.

II. BACKGROUND

In the section, it is first provided a definition of time-offset fitting with the context of GNSS/UWB hybridisation. Then, the baseline GNSS model for code-based ranging is recalled, including both pseudorange and Doppler-shift equations. Finally, a measurement model for UWB-based ranging is established which considers dynamic compensation in order to set a basis for the following time calibration implementation.

1. GNSS/UWB time-offset

Given independent rates and time-scales between GNSS and UWB clocks, an unknown time-offset exists between the timestamps of GNSS observables' and the timestamps of auxiliary UWB range measurements (Li and Mourikis, 2013).

At a generic time instant t_k - representative of estimation epoch k - in the integration time-scale, the data fusion filter processes the available GNSS and UWB observables in the measurement model (Caceres Duran et al., 2012). Accordingly, two unknown quantities can be defined:

- $\delta t_{G,k}$ identifies the lag between the set of GNSS measurements (timestamped in the GNSS time-scale) and t_k;
- $\delta t_{U,k}$ identifies the lag between the set of UWB measurements (timestamped in the UWB time-scale) and t_k;

Given so, the GNSS/UWB time-offset is defined as:

$$t_{d,k} = \delta t_{U,k} - \delta t_{G,k} \tag{1}$$

and expresses the misalignment between the timestamps of UWB measurements - tagged to the UWB time-scale - and the timestamps of GNSS measurements, with respect to the GNSS time-scale. The time-offset $t_{d,k}$ can be either a positive or a negative quantity at any epoch.

More in depth, $t_{d,k}$ accounts for two time-dependent effects:

- the relative misalignment between the GNSS and UWB measurements due to the different sampling rates and clocks of the independent sensors;
- the lag of GNSS and UWB time-scales with respect to the time-scale of the centralized unit running the GNSS/UWB tight integration algorithm.

While the former effect also involves unmodelled disturbances of independent sensor clocks (e.g., clock drift), the latter effect is contributed by data-transfer latencies, hardware-level processing and software overhead in the centralised processing unit. Moreover, assuming high measurement sampling rate for UWB and small drifts of sensor clocks, $t_{d,k}$ can be modelled as a constant between consecutive estimation epochs. Hence, in a recursive filtering set-up (Anderson and Moore, 2012), the a-posteriori time-offset estimate can be propagated as the time-offset prediction at following estimation epoch.

A graphical interpretation of the described framework is provided in Fig. 1. The three subplots are referred to the integration time-scale which, for ease of interpretation, is assumed aligned to the GNSS time-scale. In fact, $\delta t_{G,k}$ can be neglected without loss of generality if at least from one of the sensors the measurements are provided at high rate (which is typically the case of auxiliary UWB ranges), and the processing of observables in the integration filter takes place at a time t_k at which the low-rate measurements (i.e., GNSS observables) are available. In particular, the top and middle subplots of Fig. 1 show the instants at which GNSS and UWB measurements are dumped, respectively, and highlight the relative offset between GNSS and UWB time-scales. The bottom subplot, then, shows which measurements the integration filter is processing. In this work, the aim is to directly estimate $t_{d,k}$ as part of the system state, hence proposing a low complexity strategy that well fits with the GNSS/UWB tight integration framework.

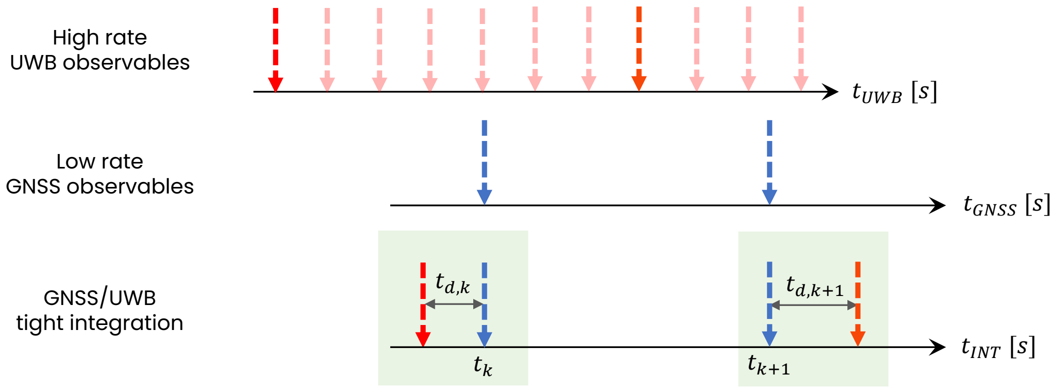

Figure 1: Illustration of the time-offset between GNSS observables and auxiliary UWB ranging measurements involved in the analysed tight integration scheme. For readability, GNSS time axis (middle) is assumed aligned to the integration time axis (bottom).

2. GNSS measurement model

The distance information from each navigation satellite to the GNSS receiver is the main component of pseudorange measurements, which also contain noises from clock bias, atmospheric delay, and other impairments affecting GNSS signal propagation (Kaplan and Hegarty, 2017). Accounting for a tracked satellite i at epoch k, the pseudorange measurement equation is formulated as (Misra and Enge, 2010):

$$\rho_{G,k}^{(i)} = \underbrace{\sqrt{(x_{G,k}^{(i)} - r_{x,k})^2 + (y_{G,k}^{(i)} - r_{y,k})^2 + (z_{G,k}^{(i)} - r_{z,k})^2}}_{r_k^{(i)}} + \delta t_{u,k} + \epsilon_k^{\rho_G^{(i)}} \tag{2}$$

where:

- $r_k^{(i)}$ is the true range between satellite i and the GNSS receiver at epoch k;
- $\boldsymbol{r}_{G,k}^{(i)} = \left(x_{G,k}^{(i)}, y_{G,k}^{(i)}, z_{G,k}^{(i)}\right)$ is the position vector of GNSS satellite i at epoch k in Earth-Centred Earth-Fixed (ECEF) coordinates;
- $\boldsymbol{r}_{u,k} = (r_{x,k}, r_{y,k}, r_{z,k})$ is the receiver position vector at epoch k in ECEF coordinates;
- $\delta t_{u,k}$ is the receiver clock bias at epoch k;
- $\epsilon_k^{\rho_G^{(i)}}$ accounts for both modelled errors (i.e., ionospheric and tropospheric induced delays) and unmodelled errors including multipath, receiver noise and other effects.

Another GNSS receiver measurement is Doppler-shift - or range-rate - which stems from the relative motion between each satellite and the GNSS receiver. Therefore, Doppler measurements are relevant to the estimation of both the user velocity and the receiver clock-drift. The Doppler measurement model can be derived by differentiating (2) and is proportional to the projection of the relative velocity vector on the satellite Line-of-Sight (LOS) (Misra and Enge, 2010):

$$\underbrace{\dot{\rho}_{G,k}^{(i)} - \boldsymbol{v}_{G,k}^{(i)} \cdot \boldsymbol{I}_k^{(i)}}_{d_{G,k}^{(i)}} = -\boldsymbol{I}_k^{(i)} \cdot \boldsymbol{v}_{u,k} + \delta f_{u,k} + \epsilon_k^{\dot{\rho}_G^{(i)}} \tag{3}$$

where:

- $\dot{\rho}_{G,k}^{(i)}$ is the pseudorange-rate measurement for satellite i at epoch k;
- $\boldsymbol{v}_{G,k}^{(i)} = \left(\dot{x}_{G,k}^{(i)}, \dot{y}_{G,k}^{(i)}, \dot{z}_{G,k}^{(i)}\right)$ is the velocity vector of GNSS satellite i at epoch k in ECEF coordinates;
- $\boldsymbol{I}_k^{(i)}$ is the unit orientation vector from the receiver to GNSS satellite i position at epoch k in ECEF coordinates;
- $\boldsymbol{v}_{u,k} = (v_{x,k}, v_{y,k}, v_{z,k})$ is the receiver velocity vector at epoch k in ECEF coordinates;
- $\delta f_{u,k}$ is the receiver clock drift;
- $\epsilon_k^{\dot{\rho}_G^{(i)}}$ is the combined error due to variations during the Doppler measurement interval in both modelled and unmodelled effects.

3. UWB measurement model with dynamic compensation

UWB is a high-accuracy localisation technology based on Time-Of-Arrival (TOA) ranging techniques (Sahinoglu et al., 2008). The baseline UWB ranging equation at epoch k can be written as:

$$\rho_{U,k}^{(j)'} = \sqrt{(x_{U,k}^{(j)} - r_{x,k}^{U})^2 + (y_{U,k}^{(j)} - r_{y,k}^{U})^2 + (z_{U,k}^{(j)} - r_{z,k}^{U})^2} + \epsilon_k^{\rho_U^{(j)}} \tag{4}$$

where:

- $\rho_{U,k}^{(j)'}$ is the UWB ranging measurement to the generic UWB anchor j at epoch k;
- $\boldsymbol{r}_{U,k}^{(j)} = \left(x_{U,k}^{(j)}, y_{U,k}^{(j)}, z_{U,k}^{(j)}\right)$ is the ECEF position of UWB anchor j at epoch k;
- $\boldsymbol{r}_{u,k}^{U} = \left(r_{x,k}^{U}, r_{y,k}^{U}, r_{z,k}^{U}\right)$ is the receiver ECEF position vector mapped by $\rho_{U,k}^{(j)'}$.
- $\epsilon_k^{\rho_U^{(j)}}$ is the combined error due to additive noise, Non-Line-of-sight (NLOS) propagation, and other unmodelled effects (Dardari et al., 2009).

Based on the definition of $t_{d,k}$ illustrated in Section II, at a generic time instant t_k corresponding to estimation epoch k, GNSS and UWB measurements are tagged to time-scales which are misaligned each other. It follows that the receiver position vector $\boldsymbol{r}_{u,k}^{U}$ doesn't match with the information about the receiver position $\boldsymbol{r}_{u,k}$ brought about by GNSS pseudorange measurements according to (2). In other words, as a consequence of $t_{d,k}$, the position information associated to the set of available auxiliary UWB ranges $\left\{\rho_{U,k}^{(j)}\right\}_{j=1}^{m}$ (m being the number of UWB anchors of opportunity at epoch k) is not time-aligned with the position information associated to the set of available GNSS-based pseudorange observables $\left\{\rho_{G,k}^{(i)}\right\}_{i=1}^{n}$ (n being the number of tracked GNSS satellites at epoch k).

By exploiting the continuous-time model for the time evolution of receiver motion parameters (Gustafsson et al., 2002), a relation between $\boldsymbol{r}_{u,k}$ and $\boldsymbol{r}_{u,k}^{U}$ can be built at t_k via dynamic compensation:

$$\begin{bmatrix} r_{x,k} \\ r_{y,k} \\ r_{z,k} \end{bmatrix} = \begin{bmatrix} r_{x,k}^{U} + \int_{t_k+\delta t_{U,k}}^{t_k+\delta t_{U,k}-t_{d,k}} v_x(t)dt \\ r_{y,k}^{U} + \int_{t_k+\delta t_{U,k}}^{t_k+\delta t_{U,k}-t_{d,k}} v_y(t)dt \\ r_{z,k}^{U} + \int_{t_k+\delta t_{U,k}}^{t_k+\delta t_{U,k}-t_{d,k}} v_z(t)dt \end{bmatrix} = \begin{bmatrix} r_{x,k}^{U} \\ r_{y,k}^{U} \\ r_{z,k}^{U} \end{bmatrix} + \begin{bmatrix} \varepsilon_{r_x,k} \\ \varepsilon_{r_y,k} \\ \varepsilon_{r_z,k} \end{bmatrix} = \boldsymbol{r}_{u,k}^{U} + \boldsymbol{\epsilon}_{r,k} \tag{5}$$

where the vector $\boldsymbol{\epsilon}_{r,k}$ represents the relative position displacement, extrapolated at $\boldsymbol{r}_{u,k}^{U}$, caused by $t_{d,k}$. Leveraging (5), the auxiliary UWB range to anchor j time-aligned to GNSS observables equals:

$$\rho_{U,k}^{(j)} = \sqrt{(x_{U,k}^{(j)} - \underbrace{(r_{x,k}^{U} + \varepsilon_{r_x,k})}_{r_{x,k}})^2 + (y_{U,k}^{(j)} - \underbrace{(r_{y,k}^{U} + \varepsilon_{r_y,k})}_{r_{y,k}})^2 + (z_{U,k}^{(j)} - \underbrace{(r_{z,k}^{U} + \varepsilon_{r_z,k})}_{r_{z,k}})^2} + \epsilon_k^{\rho_U^{(j)}} \tag{6}$$

and it is function of the unknown $t_{d,k}$ via the displacement $\boldsymbol{\epsilon}_{r,k}$.

III. METHODOLOGY

In this section, a convenient Discrete-Time System State Space (DSS) formulation for GNSS/UWB tight integration is proposed which supports time-offset calibration in a EKF-based recursive filtering framework (Ito and Xiong, 2000). Moreover, the error propagation of GNSS/UWB time-offset on EKF state-estimation is analysed theoretically. Eventually, the considered set-up to carry out the simulation-based experimental analysis is illustrated.

1. EKF-based filtering model with time-offset calibration

In the proposed time calibration framework fitting with an EKF-based Maximum a-Posteriori (MAP) filtering model (see Appendix VI) and tailored to GNSS/UWB tight integration, $t_{d,k}$ is parametrized in the state-vector and is estimated jointly with the other receiver states.

Specifically, the receiver state-vector is defined at estimation epoch k:

$$\boldsymbol{x}_{u,k} = \begin{bmatrix} \boldsymbol{r}_{u,k} & \boldsymbol{v}_{u,k} & \boldsymbol{a}_{u,k} & \delta t_{u,k} & \delta f_{u,k} & t_{d,k} \end{bmatrix}^T \tag{7}$$

where $\boldsymbol{a}_{u,k} = (a_{x,k}, a_{y,k}, a_{z,k})$ is the receiver acceleration vector in ECEF coordinates. Based on (7), the linear state-transition matrix for the discrete-time process model (Caceres Duran et al., 2012) can be formulated as:

$$\boldsymbol{F}_k = \begin{bmatrix} \boldsymbol{I}_{3\times3} & \boldsymbol{I}_{3\times3}\Delta t & 0.5\boldsymbol{I}_{3\times3}\Delta t^2 & \mathbf{0}_{3\times1} & \mathbf{0}_{3\times1} & \mathbf{0}_{3\times1} \\ \mathbf{0}_{3\times3} & \boldsymbol{I}_{3\times3} & \boldsymbol{I}_{3\times3}\Delta t & \mathbf{0}_{3\times1} & \mathbf{0}_{3\times1} & \mathbf{0}_{3\times1} \\ \mathbf{0}_{3\times3} & \mathbf{0}_{3\times3} & \boldsymbol{I}_{3\times3} & \mathbf{0}_{3\times1} & \mathbf{0}_{3\times1} & \mathbf{0}_{3\times1} \\ \mathbf{0}_{1\times3} & \mathbf{0}_{1\times3} & \mathbf{0}_{1\times3} & 1 & \Delta t & 0 \\ \mathbf{0}_{1\times3} & \mathbf{0}_{1\times3} & \mathbf{0}_{1\times3} & 0 & 1 & 0 \\ \mathbf{0}_{1\times3} & \mathbf{0}_{1\times3} & \mathbf{0}_{1\times3} & 0 & 0 & 1 \end{bmatrix} \tag{8}$$

being Δt the time between consecutive epochs (i.e., the time discretisation step) and $\boldsymbol{I}_{3\times3}$ being the identity matrix of order 3.

Leveraging the discrete-time process model (8) to approximate the integral involved in the computation of the displacement $\boldsymbol{\epsilon}_{r,k}$, the UWB ranging model (6) can be re-written as a function of the states in (7):

$$\rho_{U,k}^{(j)} = \sqrt{(x_{U,k}^{(j)} - (r_{x,k}^U + v_{x,k}t_{d,k} + 0.5a_{x,k}t_{d,k}^2))^2 + (y_{U,k}^{(j)} - (r_{y,k}^U + v_{y,k}t_{d,k} + 0.5a_{y,k}t_{d,k}^2))^2 + (z_{U,k}^{(j)} - (r_{z,k}^U + v_{z,k}t_{d,k} + 0.5a_{z,k}t_{d,k}^2))^2} + \epsilon_k^{\rho_U^{(j)}} \tag{9}$$

where the dependence on $t_{d,k}$ becomes explicit. Moving forward in the DSS formulation, the measurement vector at epoch k for a tight GNSS/UWB can be written as:

$$\boldsymbol{y}_k = \begin{bmatrix} \rho_{G,k}^{(1)} & \dots & \rho_{G,k}^{(n)} & d_{G,k}^{(1)} & \dots & d_{G,k}^{(n)} & \rho_{U,k}^{(1)} & \dots & \rho_{U,k}^{(m)} \end{bmatrix}^T \tag{10}$$

and embeds both raw GNSS-based pseudorange and Doppler-shift observables according to (2) and (3), respectively, as well as time-aligned auxiliary UWB ranging information agreeing with (9). Then, the linear observation matrix (Caceres Duran et al., 2012) can be obtained as:

$$\boldsymbol{H}_k = \begin{bmatrix} \boldsymbol{H}_{n\times3}^G & \mathbf{0}_{n\times3} & \mathbf{1}_{n\times1} & \mathbf{0}_{n\times1} \\ \mathbf{0}_{n\times3} & \boldsymbol{H}_{n\times3}^G & \mathbf{0}_{n\times1} & \mathbf{1}_{n\times1} \\ \boldsymbol{H}_{m\times3}^U & \mathbf{0}_{m\times3} & \mathbf{0}_{m\times1} & \mathbf{0}_{m\times1} \end{bmatrix} \tag{11}$$

In (11), $\mathbf{1}_{n\times1}$ represents a matrix with n rows and a single column in which all entries have unitary value. The term $\boldsymbol{H}_{n\times3}^G$ identifies the Jacobian matrix resulting from the first-order linearisation of (2) and (3), respectively. It can be expanded as:

$$\boldsymbol{H}_{n\times3}^G = \frac{\partial(h_1, \dots, h_n)}{\partial(r_x, r_y, r_z)} = \begin{bmatrix} \frac{-(x_G^{(1)} - r_x)}{r^{(1)}} & \frac{-(y_G^{(1)} - r_y)}{r^{(1)}} & \frac{-(z_G^{(1)} - r_z)}{r^{(1)}} \\ \frac{-(x_G^{(2)} - r_x)}{r^{(2)}} & \frac{-(y_G^{(2)} - r_y)}{r^{(2)}} & \frac{-(z_G^{(2)} - r_z)}{r^{(2)}} \\ \vdots & \vdots & \vdots \\ \frac{-(x_G^{(n)} - r_x)}{r^{(n)}} & \frac{-(y_G^{(n)} - r_y)}{r^{(n)}} & \frac{-(z_G^{(n)} - r_z)}{r^{(n)}} \end{bmatrix} \tag{12}$$

where $r^{(i)}$ is the true geometric range from the receiver to satellite i. The discrete-time index k has been dropped for ease of notation. In particular, the i-th row of $\boldsymbol{H}_{n\times3}^G$ collects the Cartesian components of the unit steering vector pointing from the receiver position to the i-th satellite position. Similarly, the term $\boldsymbol{H}^U_{m\times 3}$ is the Jacobian matrix for UWB ranging model (9) and, in row j, it collects the Cartesian components of the unit steering vector from the receiver position to the j-th UWB anchor. All in all, $\boldsymbol{H}^U_{m\times 3}$ has a similar structure to $\boldsymbol{H}^G_{n\times 3}$.

2. Theoretical analysis of GNSS/UWB time-offset impact

As a matter of fact, $t_{d,k}$ can affect the integrated filtering solution at every estimation epoch. To grasp the meaning of the previous sentence, it is useful to consider the UWB ranging model developed in Section II.3. The difference between the UWB range time-aligned to GNSS observables (6) and the nominal UWB range (4) identifies a ranging error term:

$$\epsilon^{(j)}_{\rho,U,k} = \rho^{(j)}_{U,k} - \rho^{(j)'}_{U,k} = \frac{\|\boldsymbol{\epsilon}_{r,k}\|^2 - 2(\boldsymbol{r}^{(j)}_{U,k} - \boldsymbol{r}^U_{u,k}) \cdot \boldsymbol{\epsilon}_{r,k}}{\rho^{(j)'}_{U,k} + \rho^{(j)}_{U,k}} \tag{13}$$

which, besides a positive scaling factor at the denominator, depends on two quantities:

1. the square of the position displacement $\boldsymbol{\epsilon}_{r,k}$ caused by $t_{d,k}$;
2. the inner product between $\boldsymbol{\epsilon}_{r,k}$ and the steering vector $(\boldsymbol{r}^{(j)}_{U,k} - \boldsymbol{r}^U_{u,k})$ to UWB anchor j.

Leveraging (13), the measurement vector (10) can be rewritten as:

$$\boldsymbol{y}_k = \begin{bmatrix} \rho^{(1)}_{G,k} \\ \vdots \\ \rho^{(n)}_{G,k} \\ d^{(1)}_{G,k} \\ \vdots \\ d^{(n)}_{G,k} \\ \rho^{(1)}_{U,k} \\ \vdots \\ \rho^{(m)}_{U,k} \end{bmatrix} = \begin{bmatrix} \rho^{(1)}_{G,k} \\ \vdots \\ \rho^{(n)}_{G,k} \\ d^{(1)}_{G,k} \\ \vdots \\ d^{(n)}_{G,k} \\ \rho^{(1)'}_{U,k} \\ \vdots \\ \rho^{(m)'}_{U,k} \end{bmatrix} + \begin{bmatrix} 0 \\ \vdots \\ 0 \\ 0 \\ \vdots \\ 0 \\ \epsilon^{(1)}_{\rho,U,k} \\ \vdots \\ \epsilon^{(m)}_{\rho,U,k} \end{bmatrix} = \boldsymbol{y}^{'}_k + \boldsymbol{\epsilon}_{\rho,U,k} \tag{14}$$

where $\boldsymbol{y}^{'}_k$ collects temporally misaligned GNSS and UWB measurements . According to (14), $t_{d,k}$ introduces an additive error on GNSS/UWB observation model. In view of this, and following the notation established in Appendix VI, the EKF innovation vector (Caceres Duran et al., 2012) can be written as:

$$\tilde{\boldsymbol{y}}_k = \boldsymbol{y}_k - \boldsymbol{H}_k \hat{\boldsymbol{x}}^-_k \tag{15}$$

Substituting (14) into (15), the a-posteriori state-estimate at epoch k can be obtained according to the EKF update (21):

$$\hat{\boldsymbol{x}}^+_k = \hat{\boldsymbol{x}}^-_k + \boldsymbol{K}_k \left(\underbrace{\boldsymbol{y}^{'}_k + \boldsymbol{\epsilon}_{\rho,U,k}}_{\boldsymbol{y}_k} - \boldsymbol{H}_k \hat{\boldsymbol{x}}^-_k \right) \tag{16}$$

Finally, the a-posteriori state-estimation error caused by $t_{d,k}$ can be derived from (16) as:

$$\boldsymbol{\epsilon}_{\rho,\boldsymbol{x},k} = \boldsymbol{K}_k \boldsymbol{\epsilon}_{\rho,U,k} \tag{17}$$

which shows that both $\boldsymbol{K}_k$ and the ranging error term $\boldsymbol{\epsilon}_{\rho,U,k}$ driven by $t_{d,k}$ affect the hybrid state-estimate. In particular, $\boldsymbol{K}_k$ acts as an amplifier of $\boldsymbol{\epsilon}_{\rho,U,k}$. It follows that, when the navigation filter largely relies upon the system model rather than on the measurements to perform the state-update, the norm of $\boldsymbol{K}_k$ converges to zero so that the impact of $t_{d,k}$ is mitigated. On the contrary, $\boldsymbol{K}_k$ would exacerbate the impact of $t_{d,k}$ on the hybrid navigation solution in case the filter trusted measurements at a very high level. Concerning $\boldsymbol{\epsilon}_{\rho,U,k}$, instead, it depends on $\boldsymbol{\epsilon}_{r,k}$ according to (13). In turns, $\boldsymbol{\epsilon}_{r,k}$ is function of the receiver velocity $\boldsymbol{v}_{u,k}$ according to (5). As a result, receiver kinematics are expected to drive the impact of $t_{d,k}$ on the accuracy of the GNSS/UWB tightly integrated solution.

3. Simulation-based Analysis Scenario

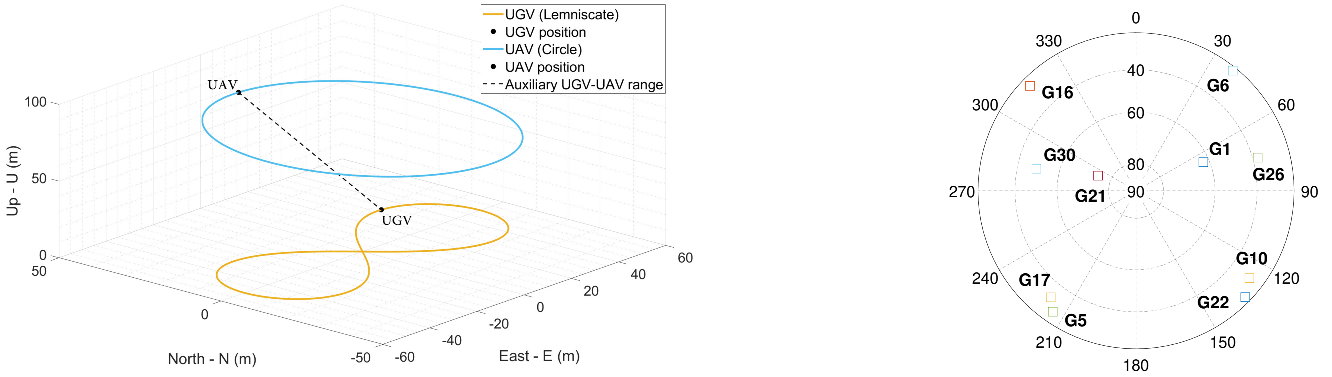

(a)

(b)

Figure 2: Experimental scenario. Simulated Bernoullian trajectory travelled by the UGV with one UWB anchor of opportunity carried on board of the UAV (a). Snapshot of satellites positions for Global Positioning System (GPS) constellation in a sky-plot diagram (b).

As anticipated earlier in Section I, this pilot study aims at investigating the proposed time-calibration methodology for GNSS/UWB tight integration in a multi-agent, cooperative scenario where the absolute UGV positioning is assisted by an UAV acting as a pseudolite supplying auxiliary UWB-based relative range measurements (i.e., a single, moving anchor of opportunity is considered). A snapshot of the addressed framework is given in Figure 2a. To carry out the experimental analysis, UGV and UAV reference trajectories are generated through a RF GNSS simulator - IFEN® Network Constellation Simulator (NCS) Titan - with $250\,\mathrm{Hz}$ positioning update rate. For the UGV, a closed-loop Bernoullian Lemniscate shape with an horizontal extension of $100\,\mathrm{m}$ is simulated which preserves a considerable variability of the observable processes. In particular, it has been centered at a reference position $(45.063981, 7.659017, 254)$ expressed as World Geodetic System 1984 (WGS84) datum. For the UAV anchor of opportunity, instead, a circular path is considered with a radius of $40\,\mathrm{m}$. In particular, it is centered at a reference position $(45.063981, 7.659017, 334)$ expressed as WGS84 datum. As a matter of fact, the relative geometry of the moving UWB anchor carried on board of UAV w.r.t. the local UGV location impacts on the instantaneous accuracy performance of the integrated navigation solution (Chen et al., 2018). Nevertheless, geometry-related considerations about optimal UAV anchor placement are out of the scope of this research and left to future studies.

For the circular UAV path, a single simulation is leveraged at $2\,\mathrm{m/s}$ average speed. For the Bernoullian UGV trajecotry, multiple simulations are run according to different average speeds: $1\,\mathrm{m/s}$, $2\,\mathrm{m/s}$, $5\,\mathrm{m/s}$, $10\,\mathrm{m/s}$, $15\,\mathrm{m/s}$, and $20\,\mathrm{m/s}$. All UGV trajectories at different average speeds are referred to the same temporal window for a time-span of 3102 epochs at $10\,\mathrm{Hz}$. The GNSS signals are generated for GPS constellation and a polar diagram of the observed satellites' distribution is given in Figure 2b. The number of visible GPS satellites is equal to 10 for the whole simulation window. Raw GPS observables are logged in RINEX format at $10\,\mathrm{Hz}$ rate (i.e., every $100\,\mathrm{ms}$) and ionospheric effects are modelled inside the GNSS simulator. Concerning UWB data, an empirical model is utilized to construct high-rate, synthetic UGV-UAV relative range measurements. Eventually, the generated datasets are post-processed via a C-language GNSS/UWB tight integration software implementing both plain EKF filtering and the proposed EKF model supporting time calibration.

IV. RESULTS

In light of the theoretical analysis developed in Section III.2, the impact of GNSS/UWB time-offset under uncalibrated tight integration via plain EKF is investigated for varying UGV kinematics in the addressed multi-agent scenario. Then, the performance of the proposed EKF-based time calibration framework is demonstrated.

1. Time-offset impact on navigation accuracy under varying kinematics

The primary goal of the following analysis is to supply a positioning error heatmap showing the way the GNSS/UWB tight integration performance is influenced both by $t_{d,k}$ and by the average receiver kinematics. The resulting error map can then be used as an indicator of the need for time calibration depending on the targeted application. To this end, with reference to the scenario discussed in Section III.3, multiple simulations of UGV trajectories at different average speeds are accounted for. Furthermore, for each post-processed UWB dataset, intentional GNSS/UWB time-offsets are introduced. For ease of notation, the discrete-time epoch index will be omitted henceforth.

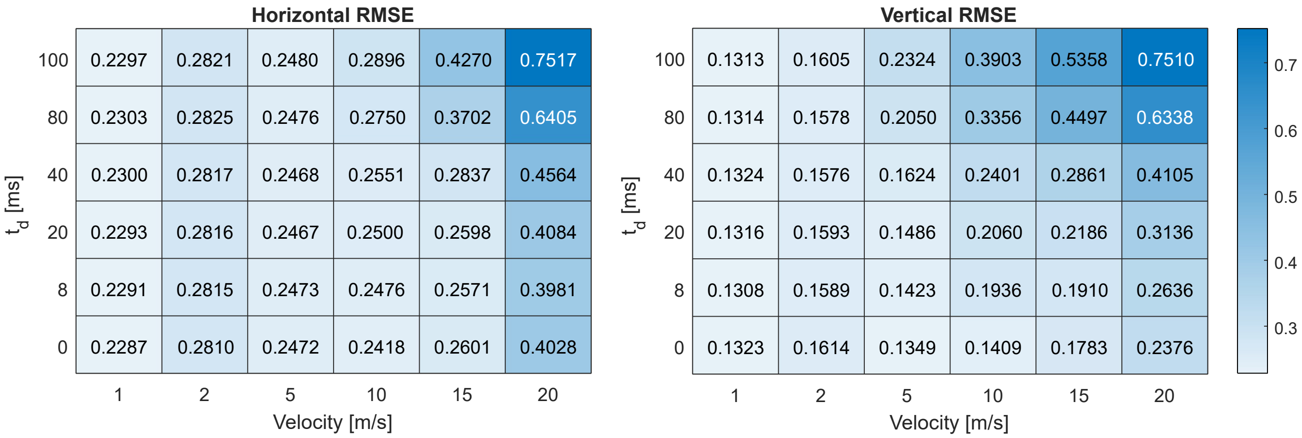

Horizontal RMSE

t_d [ms] \ Velocity [m/s]	1	2	5	10	15	20
100	0.2297	0.2821	0.2480	0.2896	0.4270	0.7517
80	0.2303	0.2825	0.2476	0.2750	0.3702	0.6405
40	0.2300	0.2817	0.2468	0.2551	0.2837	0.4564
20	0.2293	0.2816	0.2467	0.2500	0.2598	0.4084
8	0.2291	0.2815	0.2473	0.2476	0.2571	0.3981
0	0.2287	0.2810	0.2472	0.2418	0.2601	0.4028

Vertical RMSE

t_d [ms] \ Velocity [m/s]	1	2	5	10	15	20
100	0.1313	0.1605	0.2324	0.3903	0.5358	0.7510
80	0.1314	0.1578	0.2050	0.3356	0.4497	0.6338
40	0.1324	0.1576	0.1624	0.2401	0.2861	0.4105
20	0.1316	0.1593	0.1486	0.2060	0.2186	0.3136
8	0.1308	0.1589	0.1423	0.1936	0.1910	0.2636
0	0.1323	0.1614	0.1349	0.1409	0.1783	0.2376

Figure 3: Heatmap of the horizontal (left) and vertical (right) positioning RMSE in units of meter. The horizontal axis considers different average speeds of the UGV. The vertical axis, instead, considers different values of t_d.

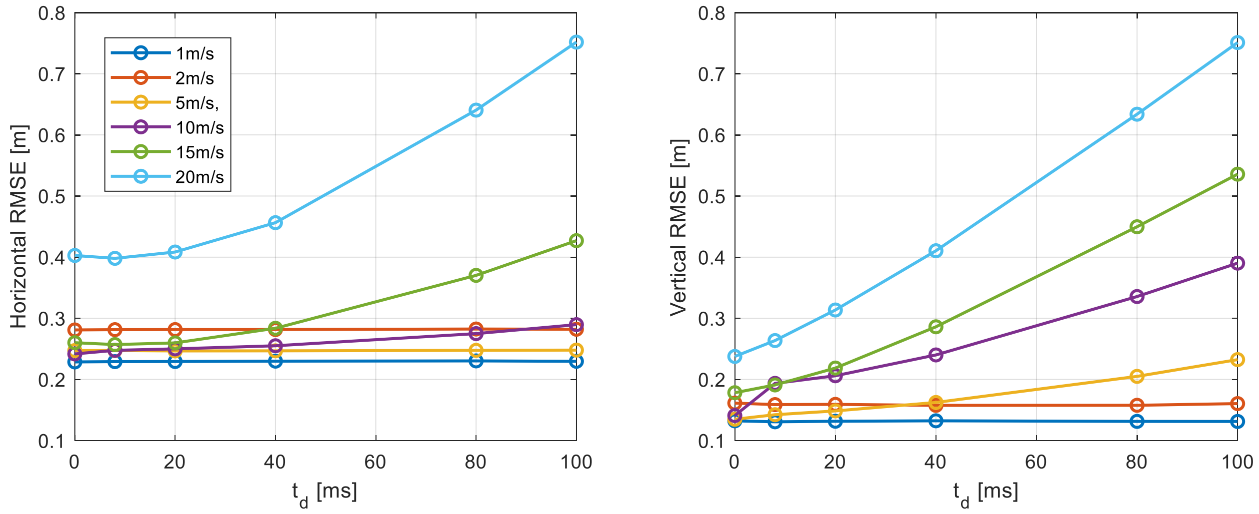

Figure 4: Horizontal (left) and vertical (right) positioning RMSE trends vs. t_d. Curves are parametrized for different UGV kinematics.

Positioning error heatmaps in Root-Mean-Square Error (RMSE) metric for both horizontal and vertical directions are shown in Figure 3. Moreover, Figure 4 displays the horizontal and vertical positioning RMSEs as a function of t_d parametrized for different UGV kinematics. In the horizontal direction, the positioning RMSE is not significantly impacted by t_d when the receiver velocity is lower than $10\,\mathrm{m/s}$. When the average speed exceeds $10\,\mathrm{m/s}$, instead, the horizontal RMSE tends to positively correlate with t_d with a nearly exponential trend. A similar behaviour can be highlighted in the vertical direction as well. Yet the positioning error is almost steady when the velocity is below $5\,\mathrm{m/s}$ for both horizontal and vertical directions.

2. GNSS/UWB tight integration statistics with/without time calibration

An experimental assessment of the presented EKF-based hybridisation methodology implementing time-offset calibration is proposed. GNSS/UWB tight integration performance is evaluated in terms of positioning accuracy statistics leveraging RMSE metric. To this end, the simulated UGV trajectory at $15\,\mathrm{m/s}$ average speed is selected which highlights relevant performance losses under uncalibrated tight integration according to Section IV.1.

In order to verify EKF-based tight integration with time calibration, a UWB ranging dataset with intentional t_d of $80\,\mathrm{ms}$ is post-processed. Figure 5a plots the time-series of the positioning error in the horizontal and vertical directions for both plain EKF integration (i.e., no time calibration) and EKF hybridisation with t_d calibration. Moreover, RMSE levels are highlighted.

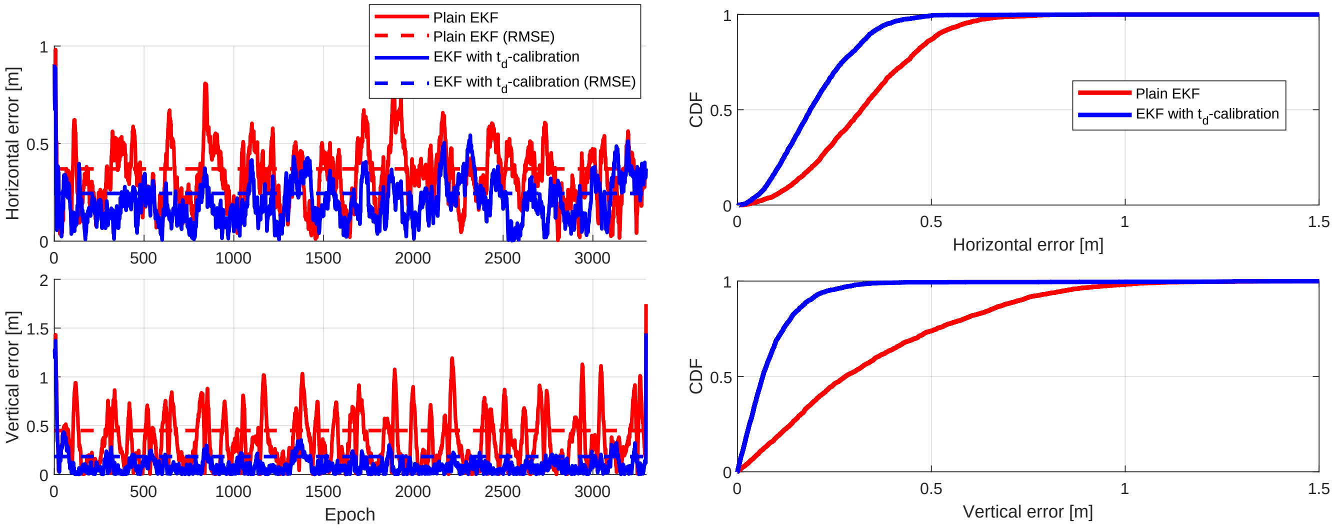

(a) **(b)**

Figure 5: Comparison of horizontal (top) and vertical (bottom) positioning error time-series for plain EKF and EKF with t_d calibration. RMSE levels are highlighted (a). Empirical Cumulative Density Function (ECDF) curves for horizontal (top) and vertical (bottom) positioning errors for plain EKF and EKF with t_d calibration (b).

Table 1: Evaluation of positioning error statistics $[\mathrm{m}]$ considering 3102 epochs (10 Hz) of PVT computation.

(a) Horizontal statistics

Tight integration filter	Error Percentile [m]		
	50-th	75-th	95-th
Plain EKF (uncalibrated)	0.3195	0.4341	0.5829
EKF with t_d-calibration	0.1874	0.2707	0.3859

(b) Vertical statistics

Tight integration filter	Error Percentile [m]		
	50-th	75-th	95-th
Plain EKF (uncalibrated)	0.2776	0.5143	0.8417
EKF with t_d-calibration	0.0651	0.1186	0.2343

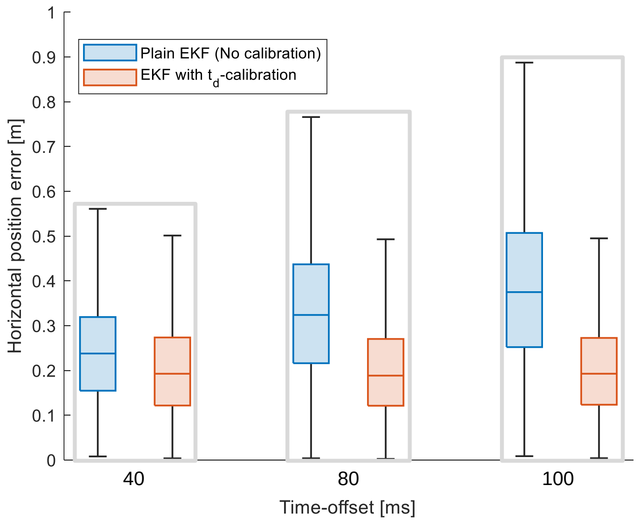

Figure 6: Positioning error box chart for t_d values of 40 ms, 80 ms and 100 ms. Comparison between plain EKF integration and EKF model with t_d calibration.

For both spatial components, the proposed time calibration framework benefits accuracy perfromance gains. In particular, in the horizontal direction, tight integration with time calibration reduces the positioning RMSE from $0.3702\,\mathrm{m}$ to $0.2445\,\mathrm{m}$, and it corresponds to an average accuracy gain of $33.95\,\%$. For the vertical direction, instead, the positioning RMSE reduces from $0.4497\,\mathrm{m}$ to $0.1829\,\mathrm{m}$, thus corresponding to a $59.33\,\%$ gain.

The ECDF lines for the horizontal and vertical positioning errors are illustrated in Figure 5b, and Table 1 summarizes both horizontal and vertical statistics at few percentiles of interest. At the 50-th percentile, the EKF model with t_d calibration achieves an accuracy gain of $41.35\,\%$ in the horizontal direction, while the gain is even bigger in the vertical direction and amounts to $76.55\,\%$. At the higher 95-th percentile, instead, the horizontal and vertical accuracy gains pursued via the the proposed time calibration EKF model are equal to $33.80\,\%$ and $72.16\,\%$, respectively.

Eventually, the box chart in Figure 6 graphically highlights the positioning accuracy improvement enabled by the proposed time calibration method for GNSS/UWB tight integration. This chart allows to emphasize the integrated positioning error for the considered filtering architectures with an indication of both the spread and skewness of the quartile distribution with respect to the median. Therefore, it comprehensively validates the improved navigation performance benefited from the proposed tight integration methodology.

V. CONCLUSION

Time-synchronisation is an established concern when addressing multi-sensor fusion with COTS chipsets, and time calibration becomes pivotal in order to enhance navigation performance under centralised, recursive filtering models. As a pilot study pertaining to the framework of GNSS/UWB tight integration for a cooperative UGV-UAV system, this work has theoretically and experimentally explored the impact of uncalibrated time-offset on the accuracy of the hybrid navigation solution when leveraging plain EKF-based data fusion. Then, an EKF-based tight integration model implementing GNSS/UWB time-offset calibration has been put forward in order to recover the navigation solution from the time-offset impact. Experimental results in the addressed multi-agent scenario highlight that the proposed time calibration method can significantly improve the accuracy of the tightly integrated navigation solution by reducing the horizontal and vertical positioning RMSEs from $0.3702\,\mathrm{m}$ to $0.2445\,\mathrm{m}$ and from $0.4497\,\mathrm{m}$ to $0.1829\,\mathrm{m}$, respectively. The improvement in positioning accuracy achieves 33.95% for the horizontal direction and 59.33% for the vertical direction. Results about the studied scenario will be of support in the context of an European Space Agency (ESA)'s Navigation Innovation and Support Program (NAVISP) project for the Proof-of-Concept (PoC) of a system enabling early-warning and persistent surveillance during disaster recovery and emergency response in Beyond Visual Line-of-Sight (BVLOS) scenarios.

VI. APPENDIX

Following the canonical EKF formulation (Julier and Uhlmann, 1997), the a-posteriori EKF state-estimate is delivered via a two-step process of prediction and update. In the prediction step, the a-priori state and covariance estimates are obtained as (Caceres Duran et al., 2012):

$$\hat{\boldsymbol{x}}_k^- = \boldsymbol{F}_{k-1}\hat{\boldsymbol{x}}_{k-1} \tag{18}$$

$$\boldsymbol{P}_k^- = \boldsymbol{F}_{k-1}\boldsymbol{P}_{k-1}\boldsymbol{F}_{k-1}^T + \boldsymbol{Q}_{k-1} \tag{19}$$

where

- $\hat{\boldsymbol{x}}_k^-$ is the a-priori state-estimate at epoch k;
- $\boldsymbol{F}_{k-1}$ is the discrete-time state-transition matrix, after linearisation of the process function around the mean a-posteriori state-estimate at previous epoch $k-1$;
- $\boldsymbol{P}_k^-$ is the a-priori state covariance estimate at epoch k
- $\boldsymbol{Q}_{\boldsymbol{k-1}}$ is the zero-mean, Gaussian multivariate process noise covariance.

Then, given the input measurement measurement vector at epoch k (i.e., $\boldsymbol{y}_k$), a correction (or update) step is run (Caceres Duran et al., 2012):

$$\boldsymbol{K}_k = \boldsymbol{P}_k^-\boldsymbol{H}_k^T(\boldsymbol{H}_k\boldsymbol{P}_k^-\boldsymbol{H}_k^T + \boldsymbol{R}_k)^{-1} \tag{20}$$

$$\hat{\boldsymbol{x}}_k^+ = \hat{\boldsymbol{x}}_k^- + \boldsymbol{K}_k(\boldsymbol{y}_k - \boldsymbol{H}_k\hat{\boldsymbol{x}}_k^-) \tag{21}$$

$$\boldsymbol{P}_k^+ = (\boldsymbol{I} - \boldsymbol{K}_k\boldsymbol{H}_k)\boldsymbol{P}_k^- \tag{22}$$

where:

- $\boldsymbol{K}_k$ is the Kalman gain matrix at epoch k;

- $\boldsymbol{H}_k$ is the discrete-time observation matrix, after linearisation of the non-linear measurement functions around the mean a-posteriori state-estimate at previous epoch $k-1$;
- $\boldsymbol{R_k}$ is the zero-mean, Gaussian multivariate measurement noise covariance;
- $\hat{\boldsymbol{x}}_k^+$ is the a-posteriori state-estimate at epoch k;
- $\boldsymbol{P}_k^+$ is the a-posteriori state covariance estimate at epoch k.

ACKNOWLEDGEMENTS

This work has been supported by the Politecnico di Torino Interdepartmental Centre for Service Robotics PIC4SeR[1] and by the Chinese Scholarship Council (CSC)[2].

REFERENCES

Anderson, B. D. and Moore, J. B. (2012). *Optimal filtering*. Courier Corporation.

Caceres Duran, M., Closas, P., Falletti, E., Fernández-Prades, C., Nájar, M., and Sottile, F. (2012). Signal Processing for Hybridization. In *Satellite and Terrestrial Radio Positioning Technique*, chapter 6, pages 317–382. Academic Press, Oxford.

Cebrian, Á., Bellés, A., Martin, C., Salas, A., Fernández, J., Arribas, J., Vilà-Valls, J., and Navarro, M. (2019). Low-cost hybrid GNSS/UWB/INS integration for seamless indoor/outdoor UAV navigation. In *Proceedings of the 32nd International Technical Meeting of the Satellite Division of The Institute of Navigation (ION GNSS+ 2019)*, pages 2680–2691.

Chen, Y., Yang, J., Trappe, W., and Martin, R. P. (2018). *Impact of Anchor Placement and Anchor Selection on Localization Accuracy*, chapter 13, pages 435–465. John Wiley & Sons, Ltd.

Cristodaro, C. (2019). *Advanced Integration of GNSS and External Sensors for Autonomous Mobility Applications*. PhD thesis, Politecnico di Torino (Turin, Italy).

Dardari, D., Conti, A., Ferner, U., Giorgetti, A., and Win, M. Z. (2009). Ranging With Ultrawide Bandwidth Signals in Multipath Environments. *Proceedings of the IEEE*, 97(2):404–426.

Ding, W., Wang, J., Li, Y., Mumford, P., and Rizos, C. (2008). Time Synchronization Error and Calibration in Integrated GPS/INS Systems. *ETRI Journal*, 30(1):59–67.

European GNSS Agency - GSA (2020). GNSS User Technology Report. Available at: https://www.euspa.europa.eu/european-space/euspace-market/gnss-market/gnss-user-technology-report.

Falco, G., Pini, M., and Marucco, G. (2017). Loose and tight GNSS/INS integrations: Comparison of performance assessed in real urban scenarios. *Sensors*, 17(2):255.

Gao, Y., Meng, X., Hancock, C. M., Stephenson, S., and Zhang, Q. (2014). UWB/GNSS-Based Cooperative Positioning Method for V2X Applications. In *Proceedings of the 27th International Technical Meeting of the Satellite Division of The Institute of Navigation (ION GNSS+ 2014)*, pages 3212–3221.

Gross, J. N., Gu, Y., and Rhudy, M. B. (2015). Robust UAV Relative Navigation With DGPS, INS, and Peer-to-Peer Radio Ranging. *IEEE Transactions on Automation Science and Engineering*, 12(3):935–944.

Gustafsson, F., Gunnarsson, F., Bergman, N., Forssell, U., Jansson, J., Karlsson, R., and Nordlund, P.-J. (2002). Particle filters for positioning, navigation, and tracking. *IEEE Transactions on Signal Processing*, 50(2):425–437.

Huang, W., Wan, W., and Liu, H. (2021). Optimization-Based Online Initialization and Calibration of Monocular Visual-Inertial Odometry Considering Spatial-Temporal Constraints. *Sensors*, 21(8).

Ito, K. and Xiong, K. (2000). Gaussian filters for nonlinear filtering problems. *IEEE transactions on automatic control*, 45(5):910–927.

Johnson, J. and Dewberry, B. (2011). Ultra-wideband Aiding of GPS for Quick Deployment of Anchors in a GPS-denied Ad-hoc Sensor Tracking and Communication System. In *Proceedings of the 24th International Technical Meeting of the Satellite Division of The Institute of Navigation (ION GNSS 2011)*, pages 3959–3966.

---

[1] https://pic4ser.polito.it/

[2] https://www.csc.edu.cn/

Julier, S. and Uhlmann, J. (2005). Fusion of time delayed measurements with uncertain time delays. In *Proceedings of the 2005, American Control Conference, 2005.*, pages 4028–4033 vol. 6.

Julier, S. J. and Uhlmann, J. K. (1997). New extension of the Kalman filter to nonlinear systems. In Kadar, I., editor, *Signal Processing, Sensor Fusion, and Target Recognition VI*, volume 3068, pages 182 – 193. International Society for Optics and Photonics, SPIE.

Kaplan, E. D. and Hegarty, C. (2017). *Understanding GPS/GNSS: principles and applications*. Artech house.

Kelly, J., Grebe, C., and Giamou, M. (2021). A Question of Time: Revisiting the Use of Recursive Filtering for Temporal Calibration of Multisensor Systems. In *2021 IEEE International Conference on Multisensor Fusion and Integration for Intelligent Systems (MFI)*, pages 1–8.

Kelly, J. and Sukhatme, G. S. (2014). *A General Framework for Temporal Calibration of Multiple Proprioceptive and Exteroceptive Sensors*, pages 195–209. Springer Berlin Heidelberg, Berlin, Heidelberg.

Li, M. and Mourikis, A. I. (2013). 3-D motion estimation and online temporal calibration for camera-IMU systems. In *2013 IEEE International Conference on Robotics and Automation*, pages 5709–5716. IEEE.

Maaref, M. and Kassas, Z. M. (2020). Ground Vehicle Navigation in GNSS-Challenged Environments Using Signals of Opportunity and a Closed-Loop Map-Matching Approach. *IEEE Transactions on Intelligent Transportation Systems*, 21(7):2723–2738.

McGraw, G. A., Groves, P. D., and Ashman, B. W. (2021). *Robust Positioning in the Presence of Multipath and NLOS GNSS Signals*, volume 1, pages 551–589. Wiley-IEEE Press.

Misra, P. and Enge, P. (2010). *Global Positioning System: Signals, Measurements, and Performance*. Ganga-Jamuna Press, 2 edition.

Morton, Y. J., van Diggelen, F., James J. Spilker, J., and Parkinson, B. W. (2020). Position, Navigation, and Timing Using Radio Signals-of-Opportunity. In *Position, Navigation, and Timing Technologies in the 21st Century: Integrated Satellite Navigation, Sensor Systems, and Civil Applications*, volume 2, pages 1115–1412. John Wiley & Sons, Inc., Hoboken, New Jersey.

Nilsson, J.-O., Skog, I., and Händel, P. (2010). Joint state and measurement time-delay estimation of nonlinear state space systems. In *10th International Conference on Information Science, Signal Processing and their Applications (ISSPA 2010)*, pages 324–328.

Peršić, J., Petrović, L., Marković, I., and Petrović, I. (2021). Spatiotemporal multisensor calibration via gaussian processes moving target tracking. *IEEE Transactions on Robotics*, 37(5):1401–1415.

Qin, T. and Shen, S. (2018). Online temporal calibration for monocular visual-inertial systems. In *2018 IEEE/RSJ International Conference on Intelligent Robots and Systems (IROS)*, pages 3662–3669.

Rehder, J., Siegwart, R., and Furgale, P. (2016). A General Approach to Spatiotemporal Calibration in Multisensor Systems. *IEEE Transactions on Robotics*, 32(2):383–398.

Sahinoglu, Z., Gezici, S., and Güvenc, I. (2008). *Ultra-wideband Positioning Systems: Theoretical Limits, Ranging Algorithms, and Protocols*. Cambridge University Press.

Skog, I. and Handel, P. (2011). Time Synchronization Errors in Loosely Coupled GPS-Aided Inertial Navigation Systems. *IEEE Transactions on Intelligent Transportation Systems*, 12(4):1014–1023.

Veth, M. J. (2021). *Nonlinear Recursive Estimation for Integrated Navigation Systems*, pages 1121–1139. Wiley-IEEE Press.

Vouch, O., Minetto, A., Falco, G., and Dovis, F. (2021). On the Adaptivity of Unscented Particle Filter for GNSS/INS Tightly-Integrated Navigation Unit in Urban Environment. *IEEE Access*, 9:144157–144170.

Win, M. and Scholtz, R. (1998). On the robustness of ultra-wide bandwidth signals in dense multipath environments. *IEEE Communications Letters*, 2(2):51–53.

Zekavat, R. and Buehrer, R. M. (2019). Wireless Localization Using Ultra-Wideband Signals. In *Handbook of Position Location: Theory, Practice, and Advances*, pages 269–301. Wiley-IEEE Press.

Zhu, N., Marais, J., Bétaille, D., and Berbineau, M. (2018). GNSS Position Integrity in Urban Environments: A Review of Literature. *IEEE Transactions on Intelligent Transportation Systems*, 19(9):2762–2778.

Zhuang, C., Zhao, H., Hu, S., Feng, W., and Liu, R. (2021). Cooperative Positioning for V2X Applications Using GNSS Carrier Phase and UWB Ranging. *IEEE Communications Letters*, 25(6):1876–1880.